

# UC Irvine

## UC Irvine Previously Published Works

### Title

Progress toward fully noninductive discharge operation in DIII-D using off-axis neutral beam injection)

### Permalink

<https://escholarship.org/uc/item/129983wd>

### Journal

Physics of Plasmas, 20(9)

### ISSN

1070-664X

### Authors

Ferron, JR  
Holcomb, CT  
Luce, TC  
[et al.](#)

### Publication Date

2013-09-01

### DOI

10.1063/1.4821072

### Copyright Information

This work is made available under the terms of a Creative Commons Attribution License, available at <https://creativecommons.org/licenses/by/4.0/>

Peer reviewed

## Progress toward fully noninductive discharge operation in DIII-D using off-axis neutral beam injection<sup>a)</sup>

J. R. Ferron,<sup>1,b)</sup> C. T. Holcomb,<sup>2</sup> T. C. Luce,<sup>1</sup> J. M. Park,<sup>3</sup> P. A. Politzer,<sup>1</sup> F. Turco,<sup>4</sup> W. W. Heidbrink,<sup>5</sup> E. J. Doyle,<sup>6</sup> J. M. Hanson,<sup>4</sup> A. W. Hyatt,<sup>1</sup> Y. In,<sup>7</sup> R. J. La Haye,<sup>1</sup> M. J. Lanctot,<sup>1</sup> M. Okabayashi,<sup>8</sup> T. W. Petrie,<sup>1</sup> C. C. Petty,<sup>1</sup> and L. Zeng<sup>6</sup>

<sup>1</sup>General Atomics, PO Box 85608, San Diego, California 92186-5608, USA

<sup>2</sup>Lawrence Livermore National Laboratory, 7000 East Ave, Livermore, California 94550-9234, USA

<sup>3</sup>Oak Ridge National Laboratory, Oak Ridge, Tennessee 37831, USA

<sup>4</sup>Columbia University, 116th St and Broadway, New York, New York 10027, USA

<sup>5</sup>University of California, Irvine, University Dr., Irvine, California 92697, USA

<sup>6</sup>University of California, Los Angeles, PO Box 957099, Los Angeles, California 90095-7099, USA

<sup>7</sup>FAR-TECH, Inc., 10350 Science Center Dr., San Diego, California 92121-1136, USA

<sup>8</sup>Princeton Plasma Physics Laboratory, PO Box 451, Princeton, New Jersey 08543-0451, USA

(Received 26 June 2013; accepted 16 August 2013; published online 11 September 2013)

The initial experiments on off-axis neutral beam injection into high noninductive current fraction ( $f_{\text{NI}}$ ), high normalized pressure ( $\beta_{\text{N}}$ ) discharges in DIII-D [J. L. Luxon, Fusion Sci. Technol. **48**, 828 (2005)] have demonstrated changes in the plasma profiles that increase the limits to plasma pressure from ideal low- $n$  instabilities. The current profile is broadened and the minimum value of the safety factor ( $q_{\text{min}}$ ) can be maintained above 2 where the profile of the thermal component of the plasma pressure is found to be broader. The off-axis neutral beam injection results in a broadening of the fast-ion pressure profile. Confinement of the thermal component of the plasma is consistent with the IPB98(y,2) scaling, but global confinement with  $q_{\text{min}} > 2$  is below the ITER-89P scaling, apparently as a result of enhanced transport of fast ions. A 0-D model is used to examine the parameter space for  $f_{\text{NI}} = 1$  operation and project the requirements for high performance steady-state discharges. Fully noninductive solutions are found with  $4 < \beta_{\text{N}} < 5$  and bootstrap current fraction near 0.5 for a weak shear safety factor profile. A 1-D model is used to show that a  $f_{\text{NI}} = 1$  discharge at the top of this range of  $\beta_{\text{N}}$  that is predicted stable to  $n = 1, 2$ , and 3 ideal MHD instabilities is accessible through further broadening of the current and pressure profiles with off-axis neutral beam injection and electron cyclotron current drive. © 2013 AIP Publishing LLC.

[<http://dx.doi.org/10.1063/1.4821072>]

### I. INTRODUCTION

Steady-state operation of tokamak reactors at high plasma pressure is anticipated to lead to improvements in the economics of fusion power production compared with pulsed operation.<sup>1</sup> In order to maintain the plasma in steady-state, the plasma current must be driven fully noninductively ( $f_{\text{NI}} = 1$ ), a constraint that is best satisfied with a large bootstrap current fraction,  $f_{\text{BS}} = I_{\text{BS}}/I_p$ , in order to minimize the power required for externally driven current. The bootstrap current fraction increases with the normalized plasma pressure,  $\beta_{\text{N}}$ , as does the fusion gain.<sup>2</sup> Future steady-state, burning plasma devices are envisioned at increasingly high values of  $\beta_{\text{N}}$ : 3.0–3.5 for the  $Q = 5$  steady-state mission of ITER,<sup>2</sup> 3.5–4.5 in a device designed to demonstrate tritium self-sufficiency [e.g., Fusion National Science Facility (FNSF)<sup>3</sup>], and 4–5 or above in a  $Q > 20$  reactor.<sup>4</sup> Given these expectations for future devices, a significant issue to resolve is the definition of parameter regimes in which MHD stable,  $f_{\text{NI}} = 1$  operation at  $\beta_{\text{N}}$  as high as 5 is possible. The focus is on low toroidal mode number ( $n = 1-3$ ) ideal MHD

instabilities in the presence of the conducting vacuum vessel wall, the modes that set the ultimate limit to plasma pressure. Here,  $\beta_{\text{N}} = 100\beta_{\text{T}}aB_{\text{T}}/I_p$  where  $\beta_{\text{T}} = 2\mu_0\langle P \rangle/B_{\text{T}}^2$ ,  $P$  is the plasma pressure,  $\langle \rangle$  indicates volume average,  $I_p$  (MA) is the plasma current,  $a$  (m) is the minor radius,  $B_{\text{T}}$  (T) is the toroidal magnetic field, and  $I_{\text{BS}}$  (MA) is the total bootstrap current.

This report describes the use of off-axis neutral beam injection and off-axis electron cyclotron current drive (ECCD) in DIII-D<sup>5</sup> to modify the current density and pressure profiles toward a regime which is expected to be stable to low- $n$  ideal MHD modes at  $\beta_{\text{N}} \approx 5$  and which is compatible with fully noninductive current drive. One reason to change from on-axis to off-axis injection for part of the neutral beam power is to broaden the profile of the neutral-beam-driven current density. This can be combined with off-axis ECCD in order to broaden the total current density profile and improve the coupling of the plasma to the conducting vacuum vessel wall, thus enhancing the effectiveness of ideal-wall stabilization of ideal low- $n$  modes. The second reason for off-axis neutral beam injection is to broaden the pressure profile, also for the purpose of improvement of stability to low- $n$  ideal modes.<sup>6-8</sup> We show that, with a broad pressure profile, the relatively low pressure gradients result

<sup>a)</sup>Paper VI3 2, Bull. Am. Phys. Soc. **57**, 366 (2012).

<sup>b)</sup>Invited speaker. Electronic mail: ferron@fusion.gat.com

in a requirement for high  $\beta_N$  in order to increase  $f_{BS}$ , leading naturally to self-consistent  $f_{NI} = 1$  solutions with  $\beta_N \approx 5$ .

In the initial experimental results with off-axis neutral beam injection into high  $f_{NI}$ , high  $\beta_N$  discharges, improved access was found to discharges with the minimum value of the safety factor,  $q_{min}$ , maintained above 2. We show that with off-axis injection and  $q_{min} > 2$ , the profile of the thermal component of the plasma pressure ( $P_{th} = n_e T_e + n_i T_i$ ) is broader. In addition, as a result of the altered deposition profile, off-axis neutral beam injection results in a broadening of the fast-ion pressure profile, the pressure of the population of unthermalized ions generated by ionization of beam injected neutrals. The calculated ideal low- $n$  stability limit to  $\beta_N$  is found to be the largest in discharges with the broadest pressure profiles. Confinement of the thermal component of the plasma, when compared to the IPB98(y,2) scaling,<sup>9</sup> is as expected for H-mode. However, global confinement with  $q_{min} > 2$  is below what is typically associated with H-mode, as determined by a comparison to the ITER-89P scaling.<sup>10</sup> This difference appears to be the result of enhanced transport of fast ions. Here,  $n_i$  and  $n_e$  are the ion and electron densities, respectively, and  $T_i$  and  $T_e$  are the ion and electron temperatures, respectively.

With guidance from the experimental results, modeling has been used to explore how increased capability for off-axis current drive in DIII-D would be used to produce discharges with, simultaneously,  $f_{NI} = 1$  and  $\beta_N \approx 5$ . Both the modeling and experimental work have focused on so-called “weak shear”  $q$  profiles. In this case, the  $q$  profile is either monotonically increasing or  $q(0) - q_{min}$  is small,  $\leq 0.5$ , and the pressure profile is relatively broad. This is in contrast with  $q$  profiles where  $q(0) - q_{min}$  is larger and there are local increases in the pressure gradient, often called an internal transport barrier (ITB). The increased pressure gradient can result in large, local bootstrap current density,  $J_{BS}$ , and thus high values of  $f_{BS}$ . However, the weak shear profile is chosen because, except in cases where the peak in the current density and the increased pressure gradients are located far from the axis,<sup>11,12</sup> increased pressure gradient generally reduces the maximum stable  $\beta_N$ .<sup>13</sup> In addition,  $J_{BS}$  can be locally larger than the total current density so that the  $q$  profile would not be constant in time. A zero-dimensional (0-D) model has been used to extrapolate from the set of previous DIII-D steady-state scenario discharges in order to study the parameter space where  $f_{NI} = 1$  solutions are available. The  $f_{NI} = 1$  solutions described here for the weak shear  $q$  profile have  $\beta_N$  approaching 5 as is desirable for a high Q reactor. This contrasts with previous studies of equilibria with the larger pressure gradients and the correspondingly high  $J_{BS}$  of an ITB-type discharge where the  $f_{NI} = 1$  solution is at relatively low  $\beta_N$ .<sup>2,14</sup> A one-dimensional (1-D) model has been used to demonstrate that a fully noninductive discharge that is predicted stable at  $\beta_N \approx 5$  is accessible in DIII-D using off-axis neutral beam and electron cyclotron (EC) heating and current drive to produce broad current and pressure profiles.

The work reported here is a continuation of previous work, in both modeling and experiment, on the use of off-axis neutral beam injection<sup>15–19</sup> and on increasing the  $\beta_N$  stability limit through broadening of the current and pressure

profiles. Modeling of the effect of broadening the pressure profile is discussed in Refs. 7 and 8. The second stable core VH-mode conceptual study<sup>11</sup> showed stability at  $\beta_N = 5.7$ . The Aries-AT steady-state reactor design<sup>4</sup> has  $\beta_N = 5.4$ , with a very low pressure peaking factor  $f_p = P(0)/\langle P \rangle = 1.93$ ,  $q_{min} = 2.4$ , and the peak current density far from the axis at normalized radius  $\approx 0.8$ . In experiments, access to  $\beta_N = 4$  through broadening of the pressure profile<sup>6</sup> and through broadening of the current profile<sup>12</sup> has been separately demonstrated in DIII-D. Modeling of stability limits to  $\beta_N$  based on the experimental results documented the benefits of broadening the current profile.<sup>12</sup>

In the remainder of this report, the first portion describes the experimental results. Section II describes the experimental setup and the analysis techniques. Section III shows the effects of off-axis injection on the  $q$ , current and pressure profiles, and Sec. IV describes confinement in these discharges. The modeling of steady-state solutions is discussed in the remainder of the report. The projected scaling of steady-state solutions from the 0-D model is described in Sec. V (additional description of the model is provided in the appendix) and the  $\beta_N \approx 5$  solution found with the 1-D model is described in Sec. VI. Conclusions are in Sec. VII.

## II. DISCHARGE PRODUCTION AND ANALYSIS

The plasmas described here were produced using the discharge shape and techniques for discharge initiation and variation of the  $q$  profile previously found to be optimum for high noninductive current fraction experiments in DIII-D<sup>20,21</sup> (an example of the discharge time evolution is shown in Fig. 1). Neutral beams at total power up to 14 MW from

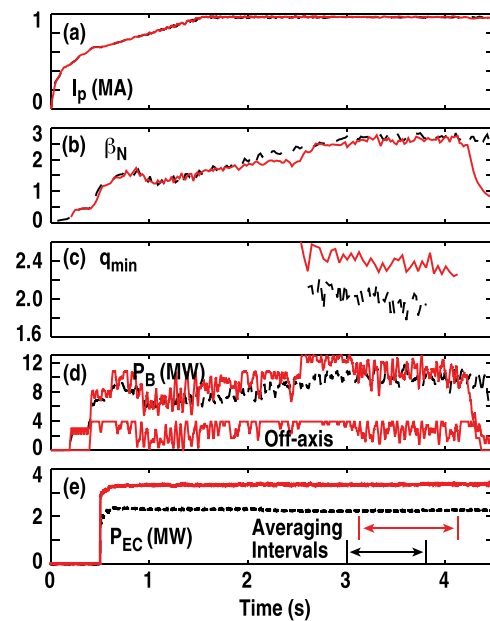


FIG. 1. Time evolution of discharges with only on-axis neutral beam injection<sup>21</sup> (dashed lines, discharge 136835) and with 25% of the power injected off-axis (solid lines, discharge 144476).  $B_T = 2.0$  T,  $q_{95} \approx 6.8$ . (a) Plasma current, (b)  $\beta_N$ , (c)  $q_{min}$  (shown only during the interval where detailed analysis was performed), (d) total and off-axis neutral beam powers (smoothed over 0.05 s, fluctuations are the result of the feedback control of  $\beta_N$ ), and (e) ECCD power, along with the averaging interval used for these discharges.

six sources that inject in the direction of the plasma current were the primary external power source. Additional heating came from gyrotron power (up to 3.4 MW) applied for ECCD in the region<sup>20</sup>  $0.25 < \hat{\rho} < 0.6$ . Here,  $\hat{\rho} = \rho/\rho_b$  is the normalized plasma radius, where  $\rho = \sqrt{\phi/\pi B_{T0}}$ ,  $\phi$  is the toroidal magnetic flux,  $B_{T0}$  is  $B_T$  at a reference major radius  $R_0$ , normally the center of the vacuum vessel, and  $\rho_b$  is the value of  $\rho$  at the discharge boundary. None of the neutral beams that inject in the direction opposite to the plasma current were used for the discharges discussed here.

A maximum of 5 MW of the neutral beam power could be injected off-axis ( $P_{\text{offaxis}}$ ) from the two neutral beam sources (contained in one beamline) that have been modified for downward vertical steering. (The injection geometry is illustrated in Refs. 22 and 23.) The vertical injection angle can be varied, but all cases with off-axis injection described here used the two off-axis sources at the maximum tilt angle, 16.4 deg, which results in a peak in the neutral-beam-driven current density ( $J_B$ ) from these sources at  $\hat{\rho}$  between<sup>19</sup> 0.4 and 0.5. In discharges where off-axis neutral beam injection was used, the direction of  $B_T$  was reversed from the standard DIII-D direction in order to maximize<sup>19</sup> the off-axis  $J_B$ . In these cases, the standard discharge shape was inverted vertically in order to maintain the ion  $\nabla B_T$  drift in the direction away from the X point.<sup>20</sup> As described elsewhere,<sup>23,24</sup> the injection geometry has been verified through imaging of  $D_\alpha$  emission from beam injection into neutral gas, and the profile of  $J_B$  from on-axis and off-axis sources has been measured in relatively low  $\beta_N < 2.3$  discharges without large-scale MHD activity such as Alfvén eigenmodes, sawteeth, or tearing modes. A good match was found between the experiment and the current density predicted by the model in the NUBEAM code.<sup>25</sup>

Except in cases where a time evolution is shown, the data presented in this report are the average of measurements or analysis at multiple time slices during the approximately constant  $\beta_N$  phase of each discharge and the error bars show the standard deviation during this averaging interval. The duration of the averaging interval is 0.12–2.8 s, depending on the discharge. The averaging interval only includes periods of the discharges without an  $n = 1$  tearing mode, but, because the focus is on discharges with relatively high  $\beta_N$ , many of the discharges do have  $n = 2$  or  $n = 3$  tearing mode activity.<sup>26</sup> Discharges are only considered if this tearing mode activity is absent or at a low amplitude. Also, as discussed further in Sec. IV, Alfvén eigenmode-type fluctuations were observed. There was no evidence of sawtooth oscillations. Following the procedure outlined in Ref. 21, equilibria were reconstructed<sup>27</sup> at 20–40 ms intervals using the measured temperature and density profiles and measurements of the magnetic field pitch angle from the motional Stark effect (MSE) diagnostic. Models implemented in the ONETWO transport code<sup>28</sup> were used to compute the bootstrap,<sup>29,30</sup> neutral-beam-driven<sup>25</sup> and EC<sup>31</sup> current densities, and the fast ion pressure profile<sup>25</sup> using the reconstructed equilibria.

Evidence for enhanced transport of the neutral-beam-injected fast ions was taken into account<sup>32</sup> in the analysis. There are no measurements of the fast ion pressure profile

available for the discharges discussed here. However, the total discharge stored energy obtained by summing the measured thermal electron and ion energies and the calculated<sup>25</sup> fast ion energy can be larger than the value from the equilibrium reconstructed using only the MSE and magnetic diagnostic data. In addition, the total measured thermal pressure plus calculated fast ion pressure at the magnetic axis can be higher than the value from the equilibrium reconstruction. These differences are interpreted as an indication that the fast ion pressure calculated from the model is larger than was actually present in the experiment. Therefore, where it is required, an assumed, radially uniform, anomalous fast ion diffusion sufficient to reduce both the pressure on axis and the total stored energy from the transport code to approximately match the values from the reconstructed equilibria was added to the neutral beam current drive calculation. The diffusion coefficient,  $0.6 < D_f < 2.0 \text{ m}^2/\text{s}$ , is larger than has been found to be necessary in previous studies of lower  $\beta_N$  discharges.<sup>15</sup> The diffusive model, although it is the best that is presently available, may not be an accurate description of the fast ion behavior in the experiment, so there is uncertainty in the exact profiles of the calculated fast ion stored energy and the neutral-beam-driven current density. Future work that would make use of the set of fast ion diagnostics<sup>23</sup> available at DIII-D to improve understanding of fast ion confinement in the type of discharge studied here is discussed in Sec. VII.

A database of steady-state scenario discharges in DIII-D has been generated from the new work reported here plus results from systematic parameter scans previously reported.<sup>20,21,26,32</sup> The database contains results obtained from scans in  $q_{\min}$ ,  $q_{95}$  ( $q$  at the 95% flux surface),  $\beta_N$ ,  $B_T$ , and the ECCD and neutral beam power deposition profiles. The plasma parameters in the database vary over a range relevant to steady-state operation in DIII-D:  $4.5 < q_{95} < 6.8$ ,  $1 < q_{\min} < 2.4$ ,  $2.6 < \beta_N < 3.9$ , line average density  $4.3 \times 10^{19} \text{ m}^{-3} < \bar{n}_e < 6.6 \times 10^{19} \text{ m}^{-3}$ ,  $1.65 \text{ T} < B_T < 2.0 \text{ T}$ , neutral beam power  $7 \text{ MW} < P_B < 14 \text{ MW}$ , ECCD power  $1.5 \text{ MW} < P_{\text{EC}} < 3.4 \text{ MW}$ , Greenwald density fraction  $0.4\text{--}0.7$ , neutral beam current drive fraction  $0.15 < f_B < 0.4$ , ECCD current drive fraction  $0.02 < f_{\text{EC}} < 0.11$ ,  $0.3 < f_{\text{BS}} < 0.6$ , and  $0.45 < f_{\text{NI}} < 0.98$ . All of the discharges in the database have the same plasma shape (except for the vertical inversion in cases with off-axis injection).

### III. MODIFICATION OF THE PLASMA PROFILES

Using the off-axis neutral beam injection capability, it has been possible to produce discharges with  $q_{\min}$  maintained above 2, even with injection of the maximum available neutral beam power, which was sufficient to reach  $\beta_N > 3$ . This is in contrast to discharges with all on-axis injection<sup>21</sup> in which  $q_{\min} \approx 1.7$  was the maximum observed at the highest injection power. The change is the result of the shift of a fraction of the neutral-beam-driven current density from on-axis to mid-radius. As an example, discharges with and without off-axis injection are compared in Fig. 1, with other parameters held constant (in particular,  $\beta_N \approx 2.7$ ). With the off-axis injection,  $q_{\min}$  is increased from 2 to 2.4, and

maintained at approximately this value for the duration of the high  $\beta_N$  phase ( $\approx 1.5$  s).

The broadening of the current density profile with off-axis injection is evident from a comparison of the discharges in the  $q_{\min}$  scan shown in Fig. 2. This set of discharges is composed of the  $q_{\min} \approx 2.4$  off-axis beam discharge shown in Fig. 1, along with the three on-axis-beam-only,  $\beta_N \approx 2.7$ ,  $q_{95} \approx 6.8$  discharges in the systematic scan described in Ref. 21. Off-axis neutral beam injection enabled the  $q_{\min}$  scan shown in Ref. 21 to be continued to a higher value [Fig. 2(a)]. As  $q_{\min}$  is increased, current density is shifted from the region near the axis to the outer half of the discharge, resulting in a broadening of the current profile [Fig. 2(b)]. This is most evident when comparing the  $q_{\min} < 2$  discharges to the two discharges with  $q_{\min} \geq 2$ . The most noticeable effect of the change to off-axis injection is the drop in the current density near the axis, with, in this example, the additional off-axis current density primarily in the H-mode pedestal region.

The scan of  $q_{\min}$  with other parameters held constant demonstrates that the thermal pressure profile broadens as  $q_{\min}$  increases. The electron temperature at mid-radius

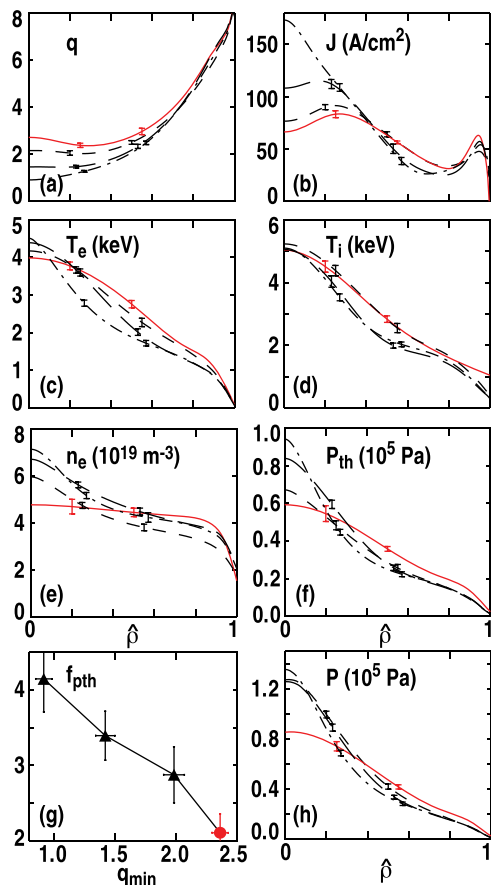


FIG. 2. Radial profiles in a scan of  $q_{\min}$ . Two of the discharges are shown in Fig. 1 (solid line: with off-axis injection, dashed line: on-axis injection only) plus there are two discharges at lower  $q_{\min}$  with on-axis injection only<sup>21</sup> (long-dashed: 136939, dotted-dashed: 136853).  $B_T = 2.0$  T,  $I_p = 0.97$  MA,  $q_{95} \approx 6.8$ ,  $\beta_N \approx 2.7$ . Radial profiles of (a) safety factor, (b) current density, (c) electron temperature, (d) ion temperature, (e) electron density, and (f) thermal pressure. (g) Thermal pressure peaking factor vs.  $q_{\min}$  (triangles: only on-axis neutral beam injection, circle: with off-axis injection). (h) Radial profile of the total plasma pressure.

increases continuously with  $q_{\min}$  and  $T_e(0)$  decreases [Fig. 2(c)]. The broadest  $T_i$  profiles are also at the largest  $q_{\min}$  [Fig. 2(d)]. A broader  $n_e$  profile with off-axis injection results partially from a decrease in  $n_e(0)$  [Fig. 2(e)], as would be expected from the decrease in the on-axis neutral beam fueling. An additional contribution comes from the increase in  $n_e$  at the H-mode pedestal that resulted from a change in the divertor strike point location that reduced the pumping of divertor exhaust.<sup>20</sup> The sum of these profile changes results in a continuous broadening of the thermal pressure profile [Fig. 2(f)] as  $q_{\min}$  increases and off-axis neutral beam injection is added. The scaling of the peaking factor for the thermal pressure,  $f_{\text{pth}} = [n_e(0)T_e(0) + n_i(0)T_i(0)]/\langle P_{\text{th}} \rangle$ , summarizes this result;  $f_{\text{pth}}$  decreases continuously as  $q_{\min}$  increases [Fig. 2(g)]. The profile of the total pressure [Fig. 2(h)], which includes the calculated fast ion pressure, also broadens.

If the  $q$  profile does not change, the thermal pressure profile does not change as a result of injection of a fraction of the beam power off-axis. This is demonstrated by the comparison of profiles for two discharges that were prepared identically except that in one of the discharges, 45% of the beam power was injected off-axis (Fig. 3). With relatively low  $q_{\min}$ , and thus relatively high current density on axis, the change in the  $J_B$  profile made little change in the  $q$  profile [Fig. 3(a)]. The density profile is slightly broader in the off-axis injection case, possibly as a result of the change in the neutral beam fueling profile [Fig. 3(b)], but the change is roughly equal to the standard deviation. The temperature profiles are nearly identical [Figs. 3(c) and 3(d)]. The

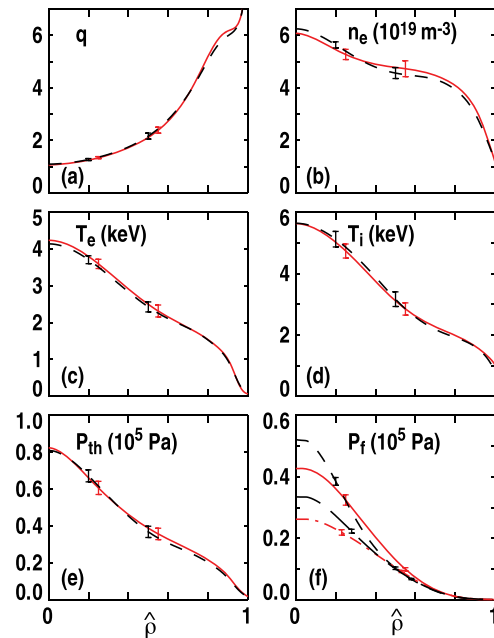


FIG. 3. Radial profiles of parameters in a discharge with on-axis injection only (dashed curves, 147380) and an otherwise identical discharge with 45% of the neutral beam power injected off-axis (solid curves, 147379). (a) Safety factor, (b) electron density, (c) electron temperature, (d) ion temperature, (e) thermal pressure, and (f) calculated fast ion pressure. In (f), the solid and dashed curves have no fast ion diffusion included in the model, while the long-dashed curve has only on-axis injection and  $D_f = 0.6$  m<sup>2</sup>/s in the model and the dot-dashed curve has off-axis neutral beam injection and  $D_f = 1.0$  m<sup>2</sup>/s.

thermal pressure profiles, then, are identical within the standard deviation [Fig. 3(e)]. The thermal pressure peaking factor,  $f_{\text{pth}} \approx 2.7$ , is lower than the  $q_{\text{min}} \approx 1$  value shown in Fig. 2(g) because<sup>21</sup>  $\beta_N$  is higher in this case,  $\approx 3.5$ .

The calculated<sup>25</sup> fast ion pressure profile broadens with off-axis injection as a result of the change in the neutral beam deposition profile. As an illustration, Fig. 3(f) includes one set of profiles that was calculated without including enhanced fast ion transport, and one set that was generated by including the appropriate fast ion diffusion coefficient in the calculation, the value determined as discussed in Sec. II. In both cases, the off-axis injection results in a broader profile, with reduced fast ion pressure on axis and, in the case with no fast ion diffusion, increased pressure at mid-radius.

The trends for the pressure peaking factors in DIII-D high  $f_{\text{NI}}$  discharges match those found from examining individual discharges (Fig. 4). At a fixed value of  $q_{\text{min}}$ , the peaking factors for both the total pressure and the fast ion pressure are the lowest for discharges, which have off-axis neutral beam injection (e.g., compare the discharges with  $1.0 < q_{\text{min}} < 1.5$ ). For  $q_{\text{min}}$  below 2, the reduction in  $f_p$  is the result of broadening of the fast ion pressure profile (Fig. 3). The lowest values for the thermal pressure peaking factor are at  $q_{\text{min}} > 2$ , in agreement with Fig. 2. As discussed in Ref. 21, the scaling of  $f_{\text{pth}}$  with  $q_{\text{min}}$  is strong at  $\beta_N \approx 2.7$ , as in Fig. 2(f), but is weak at the higher values of  $\beta_N$  shown in Fig. 4. The shaded region in Fig. 4 highlights the overall trend toward lower peaking of the total pressure at  $q_{\text{min}} > 2$ .

Broadening of the pressure profile results in an increase in the calculated  $\beta_N$  stability limit, with the highest values accessed through off-axis neutral beam injection. This is demonstrated in Fig. 5 where the calculated ideal  $n = 1$  stability limit in the presence of a perfectly conducting wall at the location of the DIII-D vacuum vessel is shown for a large fraction of the discharges in the high  $f_{\text{NI}}$  database. The width of the pressure profile is represented by  $f_p$  and the width of

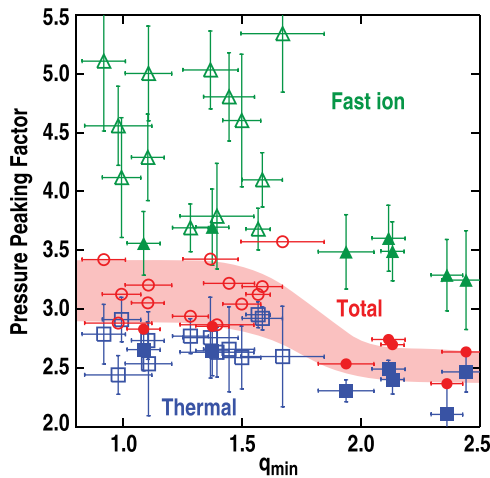


FIG. 4. The pressure peaking factors from the database of high  $f_{\text{NI}}$  DIII-D discharges described in Sec. II. The focus is on the higher  $\beta_N$  discharges with the  $\beta_N \approx 2.7$  discharges from the  $q$  profile scan discussed in Ref. 21 not shown. Open symbols: only on-axis neutral beam injection, solid symbols: with off-axis injection. Triangles: fast ion pressure ( $f_{\text{pI}}$ ), squares: thermal pressure ( $f_{\text{pth}}$ ), and circles: total pressure ( $f_p$ ). The shaded area highlights the trend toward lower  $f_p$  at higher  $q_{\text{min}}$ .

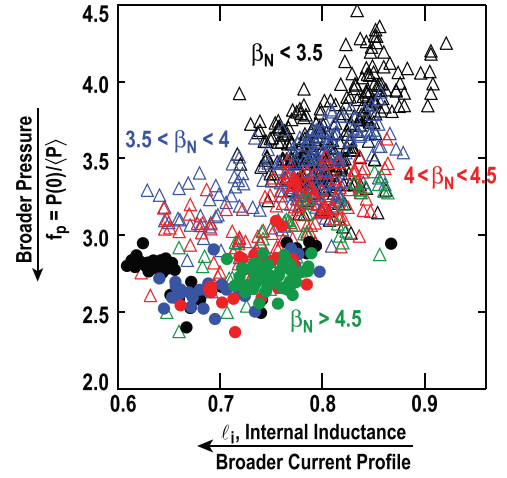


FIG. 5. The locations of equilibria from the high  $f_{\text{NI}}$  database as a function of the pressure peaking factor and the internal inductance with the corresponding range of the  $\beta_N$  stability limit. Each symbol represents an equilibrium from a single time slice in one of the discharges in the database, with multiple time slices included for each discharge. Open triangles: only on-axis neutral beam injection, closed circles: with off-axis injection. The colors indicate the range of the  $n = 1$  ideal-wall  $\beta_N$  stability limit. Black:  $\beta_N < 3.5$ , blue:  $3.5 < \beta_N < 4.0$ , red:  $4.0 < \beta_N < 4.5$ , and green:  $\beta_N > 4.5$ .

the current profile is characterized by the internal inductance ( $l_i$ ), with larger values indicating more peaked profiles. The cases with  $l_i > 0.7$  follow the pattern of a progression in the  $\beta_N$  limit from less than 3.5 at the largest values of  $f_p$  to above 4.5 with the broadest pressure profiles. For the stability limit to be above  $\beta_N = 4.5$ ,  $f_p < 3$  is required. That region is primarily populated with equilibria from off-axis neutral beam injection discharges. In order to estimate the  $\beta_N$  at the stability limit, test equilibria were produced using the TEQ equilibrium code<sup>33</sup> with the same  $q$  profile and discharge shape as in the experimental equilibria, but with the pressure profile scaled by a factor that is constant as a function of radius. For each new equilibrium, the  $n = 1$  stability was calculated using the DCON code<sup>34</sup> and the scale factor was iterated to find a marginally stable equilibrium.

For the discharges produced thus far with off-axis neutral beam injection, the current profile has not been sufficiently broadened that an increase in the  $\beta_N$  stability limit through improved ideal-wall stabilization could be demonstrated. There is a trend to lower  $l_i$  as  $f_p$  decreases and the  $n = 1$  ideal-wall  $\beta_N$  limit increases (Fig. 5), but the off-axis cases with the broadest current profiles,  $l_i < 0.7$  where  $q_{\text{min}} > 2$ , have the  $\beta_N$  limit below 4. In contrast, the lowest  $f_p$  equilibria with  $l_i > 0.7$  have  $q_{\text{min}} \leq 1.5$  and the  $\beta_N$  limit is primarily above 4.5. This is consistent with expectations for the ideal  $n = 1$  stability limit. With insufficient ideal-wall stabilization, the limit decreases with increasing<sup>6,12</sup>  $q_{\text{min}}$  and decreasing<sup>7</sup>  $l_i$ . It is likely that for the lowest  $l_i$  equilibria in Fig. 5, the conducting wall is not sufficiently close to the plasma for its stabilizing effect to overcome the destabilizing effect of a low value of  $l_i$  and a high value of  $q_{\text{min}}$ . If an improvement in wall stabilization is simulated by calculating the stability limit using a conformal wall (i.e., with the same shape as the plasma) located at  $1.35a$ , the  $\beta_N$  stability limit is increased to above 4 for most of the equilibria with  $l_i < 0.7$ .

(The DIII-D vacuum vessel is equivalent to a conformal wall at approximately  $1.42a$ .) This leads to the plans for DIII-D to improve wall stabilization to enable stable operation with  $\beta_N \approx 5$  by further broadening the current density profile, as discussed in Sec. VI.

#### IV. CONFINEMENT

Although the broader pressure profiles obtained with off-axis neutral beam injection lead to the expectation of higher stability limits, the highest  $\beta_N$  obtained with  $q_{\min} \geq 2$  thus far is 3.3. The maximum  $\beta_N$  is limited by confinement and the maximum available neutral beam power rather than ideal low- $n$  MHD stability, although, as noted in Sec. III, plasmas with the broadest current profiles may have been close to the stability boundary.

Steady-state scenario discharges have confinement of the thermal pressure at the level expected for a typical H-mode [Figs. 6(a) and 6(b)]. The figure shows the ratio of the thermal energy confinement time ( $\tau_{\text{Eth}}$ ) to  $\tau_{98}$ , the confinement time predicted by the IPB98(y,2) energy confinement scaling.<sup>9</sup> This value is referred to here as  $H_{98}$ , the H-mode confinement scaling factor, although here the thermal energy confinement time is determined from the measured thermal pressure profile integrated over the plasma volume ( $W_{\text{th}}$ ). The value of  $H_{98}$  is usually determined for DIII-D by subtracting an estimate of the fast ion stored energy from the total stored energy obtained from an equilibrium reconstruction using the EFIT<sup>27</sup> code ( $W_{\text{MHD}}$ ). This value of  $H_{98}$  should be equal to the value computed from  $\tau_{\text{Eth}}$  within the uncertainties in stored energy values determined from the measurement of the thermal pressure profile, the estimate of the fast ion stored energy, and the equilibrium reconstruction. The method used here was chosen because of the evidence for enhanced fast ion transport in the experiment that increases the uncertainty in the calculation of the

fast ion stored energy. For H-mode,  $H_{98} = 1$  would be expected, while most of the discharges shown in the figure are clustered around  $H_{98} \approx 1.2$ , with some cases having somewhat higher values. Both in a scan of  $q_{\min}$  with other parameters held constant [Fig. 6(a)] and in the full database [Fig. 6(b)], there is no systematic trend observed with  $q_{\min}$  or a systematic difference between discharges with and without off-axis injection.

The highest  $q_{\min}$  plasmas have global (i.e., thermal plus fast ion) confinement below the typical H-mode level [Figs. 6(c) and 6(d)]. The value of the  $H_{89}$  confinement scaling factor<sup>10</sup> typically associated with H-mode is approximately 2. At the lowest values of  $q_{\min}$ , DIII-D high  $f_{\text{NI}}$  discharges have  $H_{89}$  above this value, as shown in the figure for both the single parameter  $q_{\min}$  scan [Fig. 6(c)] and for the full database [Fig. 6(d)]. However, there is a trend toward  $H_{89} < 2$  at  $q_{\min} > 2$ . Discharges with  $q_{\min} > 2$  and off-axis neutral beam injection have  $H_{89}$  as low as 1.65. It is these low values of  $H_{89}$  that have thus far limited the achievable value of  $\beta_N$  with  $q_{\min} > 2$ .

A change in the neutral beam injection location to off-axis results in only a small reduction in the global confinement, as demonstrated by a comparison of the two discharges shown in Fig. 3. This confinement decrease can be understood as resulting from neutral beam deposition in a region that is closer to the plasma boundary; and in that region, the thermal diffusivity is higher. The two discharges have the same  $\beta_N \approx 3.5$ , and have nearly the same  $q$ , temperature and density profiles (Fig. 3). The discharge with 45% of the neutral beam power injected off-axis during the high  $\beta_N$ , relatively stationary portion of the discharge, required an increase in the total neutral beam power of 13% over that required for the discharge which had only on-axis injection. With 2.8 MW ECCD power also present in both cases, this translates to a reduction in energy confinement time of 10% and a reduction in  $H_{89}$  of only 5% (as the  $H_{89}$  scaling includes the square root of the heating power  $P_{\text{H}} = P_{\text{B}} + P_{\text{EC}}$ ). This reduction in  $H_{89}$  is much less than the difference between the low and high  $q_{\min}$  discharges in Figs. 6(c) and 6(d).

Because the confinement of the thermal energy is as expected for H-mode and shows no evidence of scaling with  $q_{\min}$ , the decrease in global confinement with  $q_{\min}$  is interpreted as resulting from increased fast ion transport as  $q_{\min}$  increases. It is possible that fast-ion-driven instabilities are causing fast ion transport, and consistent with this is the observation that the fluctuation power in the Alfvén eigenmode frequency range,<sup>35</sup>  $f > f_{\text{TAE}} = v_A / (4\pi qR)$ , increases as a function of  $q_{\min}$  for discharges in the high  $f_{\text{NI}}$  database (Fig. 7). Here,  $v_A = B_T / \sqrt{\mu_0 \rho_m}$  is the Alfvén velocity where  $\rho_m$  is the ion mass density.

#### V. SCALING OF FULLY NONINDUCTIVE SOLUTIONS

In this section, a relatively simple 0-D model, yielding primarily global values, is used to describe the features of the parameter space where  $f_{\text{NI}} = 1$  is accessible in DIII-D. The primary motivation is to define the conditions where fully noninductive operation is compatible with  $\beta_N = 5$  or above, as is desirable in a reactor. This compatibility does

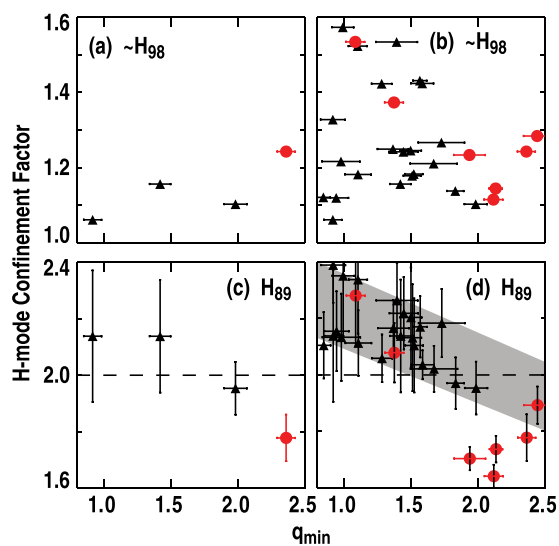


FIG. 6. H-mode confinement scaling factors from the DIII-D steady-state discharge database: (a) and (b)  $W_{\text{th}}/P_{\text{H}}/\tau_{98} \approx H_{98}$  for thermal confinement, (c) and (d)  $H_{89} = W_{\text{MHD}}/P_{\text{H}}/\tau_{89}$  for global confinement.<sup>10</sup> (a) and (c) Only the discharges in Fig. 2. (b) and (d) The full database. Triangles: only on-axis neutral beam injection; and circles: with off-axis injection.

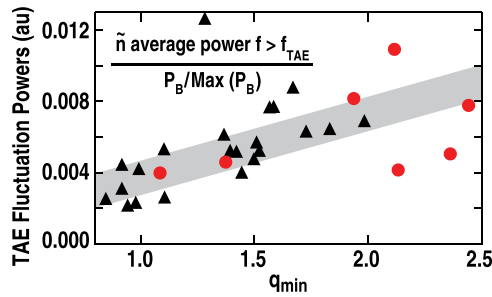


FIG. 7. For the discharges in the DIII-D high  $f_{\text{NI}}$  discharge database, the average electron density fluctuation power in the range of frequencies above  $f_{\text{TAE}}$  normalized to the ratio of the neutral beam power in each discharge to the maximum neutral beam power in all discharges in the database. Triangles: only on-axis neutral beam injection; and circles: with off-axis injection.

not occur with arbitrary plasma parameters because a balance is required between the confinement and heating that determines the plasma pressure and the bootstrap current fraction, and the input power required for externally driven current, which also heats. We show that with a broad pressure profile,  $f_{\text{NI}} = 1$  is projected at  $\beta_{\text{N}} > 4$ , but that steeper pressure gradients yield fully noninductive solutions at lower values of  $\beta_{\text{N}}$ . Thus, the use of off-axis neutral beam injection to broaden the plasma profiles and increase the stability limits to plasma pressure, as in the experiments described here, is also consistent with achieving steady-state operation. Although fully noninductive conditions have been produced previously<sup>20,36</sup> in DIII-D with on-axis neutral beam injection, in these initial off-axis injection experiments, the noninductive fraction was in the range  $0.65 < f_{\text{NI}} < 0.8$ . In order to enable a systematic approach to producing fully noninductively driven discharges, we also describe predictions from the model for how the locations in parameter space where  $f_{\text{NI}} = 1$  scale with  $q_{95}$ ,  $B_{\text{T}}$ , and  $n_e$ , and the effects of increasing the fraction of the neutral beam power deposited off-axis or the fraction of electron cyclotron power. The predicted values of  $f_{\text{BS}}$  are also examined and are contrasted with what is expected to be achievable in a reactor.

The task in searching for a steady-state operating point using the 0-D model is to find a set of the externally selectable discharge parameters that results in  $f_{\text{NI}}$  exactly 1. Once the tokamak geometry has been determined (including the plasma shape and size), the set of externally selectable parameters is limited. Available for modification are  $\beta_{\text{N}}$ ,  $q_{95}$ ,  $B_{\text{T}}$ , settings that affect the external particle fueling and divertor exhaust pumping rates and thus the plasma density, settings that determine the deposition profile of the external current drive power, and the types of the external heating sources. Other parameters are determined self consistently by the plasma.

Given a set of the externally selectable parameters, the 0-D model provides values for the noninductive current fractions  $f_{\text{BS}}$ ,  $f_{\text{B}}$ , and  $f_{\text{EC}}$ , as described in the appendix. The model extrapolates from the existing database of DIII-D steady-state scenario discharges (Sec. II), including cases both with and without off-axis neutral beam injection. The database contains discharges with a range of parameters (e.g.,  $q_{\text{min}}$ ,  $q_{95}$ ,  $\beta_{\text{N}}$ ,  $f_{\text{BS}}$ ,  $f_{\text{NI}}$ ) sufficiently broad that the model

is well validated and the extrapolations necessary to study steady-state solutions are of reasonable range. The plasma pressure is found by using the IPB98(y,2) global confinement scaling<sup>9</sup> to determine the thermal plasma pressure, and the fast ion pressure is obtained from a model that uses as input the neutral beam power and estimates of  $n_e$  and  $T_e$ . The noninductive current fractions are determined from theory-based analytic models with coefficients that are determined from fits to the experimental database. The fitting coefficients implicitly characterize the temperature and density profiles typical of the DIII-D discharges. Other parameters that are inputs to the model are chosen to match the experimental results. In particular,  $H_{98} = 1.2$  is used here, as is appropriate for most of the database (Fig. 6). The pressure peaking factors for the inner ( $f_{\text{pi}}$ ) and outer ( $f_{\text{po}}$ ) portions of the profile (defined in the appendix) are chosen to characterize the differences between discharges with and without off-axis neutral beam injection (Sec. III). The broadening of the thermal pressure profile as a result of the increase in  $q_{\text{min}}$  with off-axis injection results in lower values of  $f_{\text{pi}}$  and slightly increased  $f_{\text{po}}$ . Similarly, the  $T_i$  to  $T_e$  ratio near the axis increases with off-axis injection as a result of the broadening of the  $T_e$  profile. The model provides an estimate of the average current density and  $q$  near the axis, but otherwise cannot predict the complete current density profile.

A single  $f_{\text{NI}} = 1$  operating point can be found through a scan of one of the adjustable model input parameters with the other input parameters held fixed. An example is shown in Fig. 8, where the scanned parameter is  $\beta_{\text{N}}$ , the parameter on which  $f_{\text{NI}}$  is most strongly dependent. The IPB98(y,2) thermal confinement model and the fast ion pressure model are used to determine the required  $P_{\text{H}}$  at each value of  $\beta_{\text{N}}$  [Fig. 8(a)]. Here,  $P_{\text{EC}}$  is held constant at the maximum that has been available at DIII-D, with neutral beams providing the remainder of the input power. Application of the constraint that the current drive power ( $P_{\text{CD}}$ ) is equal to the heating power, as is the case in DIII-D experiments, then yields the noninductive current fractions [Fig. 8(b)], and a single value of  $\beta_{\text{N}}$  where  $f_{\text{NI}} = 1$  (circled in Fig. 8). The bootstrap current fraction increases with  $\beta_{\text{N}}$  as a result of the increase in the self-consistent value of  $q_{\text{core}}$  [Fig. 8(c)] (the average value of  $q$  in the region  $0 < \hat{r} < 0.3$ ) and the increase in  $\beta_{\text{Nth}}$ , the component of  $\beta_{\text{N}}$  resulting from the thermal plasma pressure [Fig. 8(d)]. The value of  $q_{\text{core}}$  increases because, near the axis, the inductive current density drops more rapidly than the increase in the bootstrap and neutral-beam-driven current densities. The external current drive fraction [ $f_{\text{CD}} = f_{\text{B}} + f_{\text{EC}}$ , Fig. 8(b)] increases with the input power and  $T_e$  which rises as the stored energy increases at constant line average density.

The parameter space for  $f_{\text{NI}} = 1$  operation is determined by calculating a continuum of solutions. As an illustration, Fig. 9 shows parameters at  $f_{\text{NI}} = 1$  as a function of  $q_{95}$ . At each value of  $q_{95}$ ,  $\beta_{\text{N}}$  was scanned in order to find the value at which  $f_{\text{NI}} = 1$ . Other parameters provided as input to the model were held fixed at values that are appropriate for weak shear profile DIII-D discharges. The line average electron density is held fixed at a value that is typical of what can be obtained in DIII-D with fueling from high-power neutral

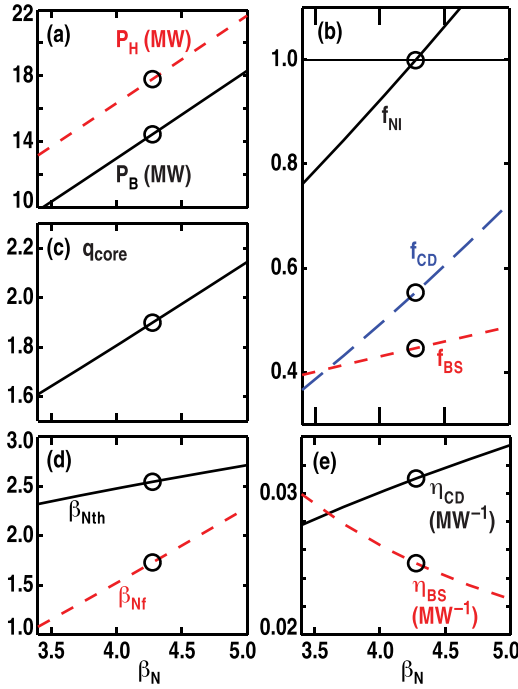


FIG. 8. Output of the 0-D model. (a) The required total heating (dashed curve) and neutral beam (solid curve) powers, (b)  $f_{NI}$  (solid curve),  $f_{BS}$  (dashed curve),  $f_{CD}$  (long-dashed curve), (c)  $q_{core}$ , (d)  $\beta_{Nth}$  (solid curve), and  $\beta_{Nf}$ , the component of  $\beta_N$  resulting from the fast ion pressure (dashed curve), (e)  $\eta_{BS} = f_{BS}/P_H$  (dashed line),  $\eta_{CD} = f_{CD}/P_{CD}$  (solid line). The circles highlight the values when  $f_{NI} = 1$ . Values of the fixed parameters for the model are also used for Fig. 9 through 12 unless specifically mentioned in the caption:  $q_{95} = 5.75$ ,  $P_{offaxis} = 5.0$  MW,  $P_{EC} = 3.35$  MW, neutral beam voltage 77 kV,  $B_T = 1.75$  T,  $f_{pi} = 1.05$ ,  $f_{po} = 1.3$ ,  $Z_{eff} = 1.8$ ,  $T_i(0.13)/T_e(0.13) = 1.45$ ,  $D_f = 0$ ,  $H_{98} = 1.2$ ,  $\rho_{EC} = 0.45$ ,  $\bar{n}_e = 4.5 \times 10^{19} \text{ m}^{-3}$ .

beam injection and cryopumping of divertor exhaust. Similarly, the locations of the  $f_{NI} = 1$  operating point as a function of  $B_T$ ,  $n_e$  and  $P_{EC}$  are shown in Figs. 10–12.

The bootstrap current fraction [Figs. 8(b) and 9(c)] is limited to a value near 0.5 as a result of the use of external heating sources that also efficiently drive current and the broad pressure profile characteristic of the weak shear discharges studied here. At  $f_{NI} = 1$ , the division between bootstrap current and externally driven current is determined by the relative magnitudes of the efficiency of current fraction generation by the heating and current drive powers,  $\eta_{BS} = f_{BS}/P_H$  and  $\eta_{CD} = f_{CD}/P_{CD}$ . Using the 0-D model for  $f_{BS}$  (appendix) yields

$$\eta_{BS} = \frac{4 \mu_0 a \tau_{Eth}}{3 B_T I_p V} (C_1 q_{core} f_{pi}^{C_2} + C_3 q_{95} f_{po}^{C_4}), \quad (1)$$

where  $V$  is the plasma volume. With the assumption that the IPB98(y,2) thermal energy confinement time scaling holds,  $\tau_{Eth} \propto H_{98} P_H^{-0.69}$  so that  $\eta_{BS}$  decreases rapidly as the heating power is increased in order to increase  $\beta_N$  [Fig. 8(e)]. In contrast, from the scaling relations in the appendix,  $\eta_{CD} \propto T_e/n_e$  so that it is independent of the input power and increases with  $\beta_N$  because  $T_e$  rises [Fig. 8(e)]. As a result,  $\eta_{CD}$  is comparable to or larger than  $\eta_{BS}$  and, at  $f_{NI} = 1$  with  $P_H = P_{CD}$ ,  $f_{BS} = 1/(1 + \eta_{CD}/\eta_{BS})$  is 0.5 or below.

For efficient steady-state operation, it is desirable to maximize  $f_{BS}$  and there are several ways to increase its value

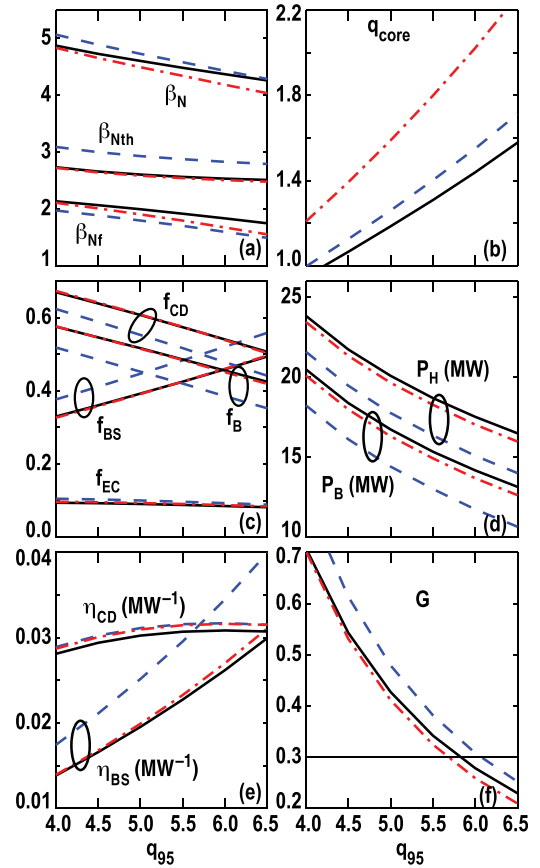


FIG. 9. Parameters at the  $f_{NI} = 1$  operating point as a function of  $q_{95}$  from the 0-D model. (a)  $\beta_N$ ,  $\beta_{Nth}$ , and  $\beta_{Nf}$ , (b)  $q_{core}$ , (c) the noninductive current fractions (d) the input powers, (e)  $\eta_{BS} = f_{BS}/P_H$ ,  $\eta_{CD} = f_{CD}/P_{CD}$ , and (f)  $G = \beta_N H_{89}/q_{95}^2$ . Solid line:  $P_{offaxis} = 0$ ,  $H_{98} = 1.2$ ,  $f_{pi} = 1.35$ ,  $f_{po} = 1.25$ ,  $T_i(0.13)/T_e(0.13) = 1.22$ , dashed line:  $P_{offaxis} = 0$ ,  $H_{98} = 1.4$ ,  $f_{pi} = 1.35$ ,  $f_{po} = 1.25$ ,  $T_i(0.13)/T_e(0.13) = 1.22$ , dotted-dashed line:  $P_{offaxis} = 5.0$  MW,  $H_{98} = 1.2$ ,  $f_{pi} = 1.05$ ,  $f_{po} = 1.3$ ,  $T_i(0.13)/T_e(0.13) = 1.45$ . The solid and the dotted-dashed lines overlay each other in (c).

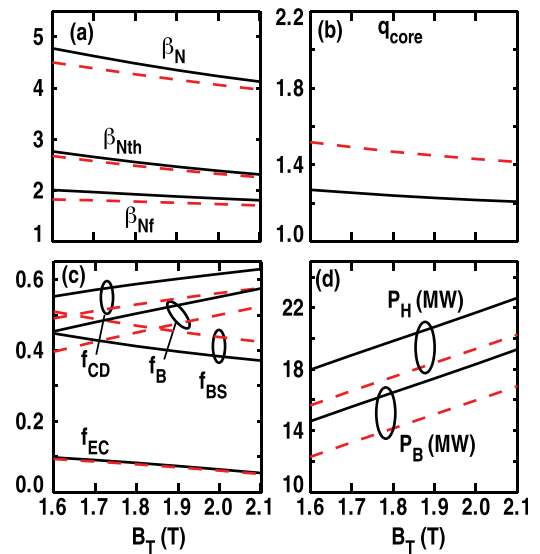


FIG. 10. Parameters at the  $f_{NI} = 1$  operating point as a function of  $B_T$  obtained using the 0-D model. (a)  $\beta_N$ ,  $\beta_{Nth}$ ,  $\beta_{Nf}$ , (b)  $q_{core}$ , (c) the noninductive current fractions, and (d) the input powers. Solid line:  $q_{95} = 5.3$ , dashed line:  $q_{95} = 6.2$ .  $P_{offaxis} = 0$ ,  $f_{pi} = 1.35$ ,  $f_{po} = 1.25$ ,  $T_i(0.13)/T_e(0.13) = 1.22$ .

by increasing  $\eta_{BS}$ . An increase in  $q_{95}$  results in an increase in  $\eta_{BS}$  at the  $f_{NI} = 1$  solution [Fig. 9(e)] and a corresponding increase in  $f_{BS}$  [Fig. 9(c)] because there is very little change in  $\eta_{CD}$  [Fig. 9(e)]. Additional contributions to the change in  $\eta_{BS}$  come from higher values of  $q_{core}$  at increased  $q_{95}$  that are a result of reduced  $P_B$  [Fig. 9(b)] and thus reduced neutral-beam-driven current density near the axis, and an increase in  $\tau_{Eth}/I_p$  with  $q_{95}$  as a result of the reduced heating power. If the assumed confinement quality is increased to  $H_{98} = 1.4$  (Fig. 9, dashed line) from 1.2 (solid line),  $f_{BS}$  increases by about 0.05. Operation at reduced  $B_T$  (Fig. 10) results in increased  $\eta_{BS}$  and  $f_{BS}$  because of the reduced heating power. Another approach to increasing  $f_{BS}$  could be an increase in the pressure gradient, which is relatively small with a weak shear  $q$  profile. An increase in the outer half of the discharge, in particular, where  $f_{po}$  is weighted by  $q_{95}$ , could make a significant change in  $\eta_{BS}$ . At the  $f_{NI} = 1$  solution, though, the effect of an increase in the pressure gradient is somewhat moderated by an accompanying decrease in  $\beta_N$  and  $\beta_{Nth}$ . With more bootstrap current, reduced external current drive power is required resulting in a drop in stored energy, so that  $f_{BS}$  does not increase as much as might have been expected from simply increasing the pressure gradient.

A larger value of  $f_{BS}$  can be obtained by increasing the electron density (Fig. 11). This is a result of a decrease in  $\eta_{CD}$  as  $\bar{n}_e$  increases [Fig. 11(d)] while  $\eta_{BS}$  is nearly constant because of a positive scaling of  $\tau_{Eth}$  with  $\bar{n}_e$  in the IPB98(y,2) scaling law. The  $f_{NI} = 1$  solution shifts to higher  $\beta_N$  and higher  $P_H$  as is required in order to replace externally driven current with bootstrap current. At the highest density shown (which approximately matches the cutoff density for the ECCD),  $f_{BS}$  is still limited to  $\approx 0.57$ , even at  $q_{95} = 6.2$ .

The projected  $f_{NI} = 1$  operating point in DIII-D has  $\beta_N$  between 4 and 5, with only weak dependence on the externally selectable discharge parameters. Increasing  $q_{95}$  reduces

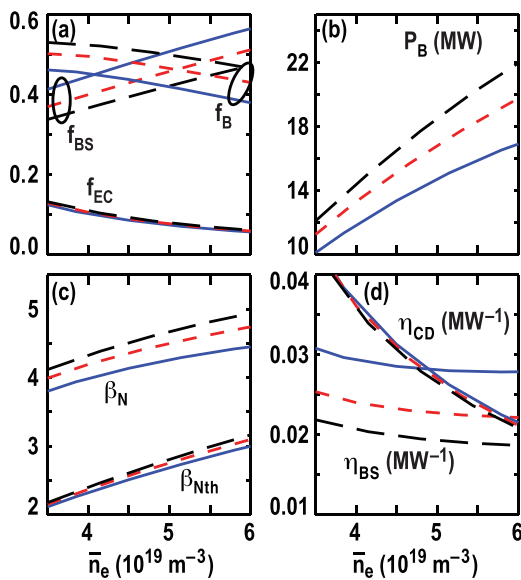


FIG. 11. Parameters at the  $f_{NI} = 1$  operating point as a function of  $\bar{n}_e$  obtained using the 0-D model. (a) The noninductive current fractions (b)  $P_B$ , (c)  $\beta_N$  and  $\beta_{Nth}$ , and (d)  $\eta_{BS} = f_{BS}/P_H$  and  $\eta_{CD} = f_{CD}/P_{CD}$ .  $q_{95} = 5.0$  (long dash), 5.5 (dashed line), and 6.2 (solid line).  $P_{offaxis} = 5$  MW,  $f_{pi} = 1.05$ ,  $f_{po} = 1.3$ ,  $T_i(0.13)/T_e(0.13) = 1.45$ .

$\beta_N$  at the solution [Fig. 9(a)] along with the required heating power, but also results in reduced  $\beta_T$  and so projects to reduced fusion gain. The requirement for the ITER  $Q = 5$  steady-state mission,<sup>2</sup>  $G = \beta_N H_{89}/q_{95}^2 = 0.3$ , is projected at  $q_{95} \approx 5.8$  in this example [Fig. 9(f)]. An increase in the assumed confinement quality (Fig. 9 dashed and solid lines) results in a decrease in the required  $P_B$  and a corresponding reduction in  $f_{CD}$  and increase in  $f_{BS}$ , but almost no change in  $\beta_N$ . Solutions at relatively low  $f_{CD}$  have relatively high  $\beta_N$  in order to produce the required  $f_{BS}$ . This is evident again in the scaling with  $B_T$  (Fig. 10) where the required heating power increases<sup>32</sup> rapidly with  $B_T$ , resulting in an increase in  $f_{CD}$ , a decrease in  $f_{BS}$ , and a decrease in  $\beta_N$  at the  $f_{NI} = 1$  solution. The increase in  $P_B$  results in a drop in  $q_{core}$  with  $B_T$  [Fig. 10(b)] because the neutral-beam-driven current density increases near the axis.<sup>32</sup> This increase is partly compensated, though, by a drop in the bootstrap current density near the axis so the rate of change of  $q_{core}$  with  $B_T$  is small.

Fast ions account for a large fraction of the total stored energy, contributing to the relatively high  $\beta_N$  at  $f_{NI} = 1$  [Figs. 8(d), 9(a), and 10(a)]. Because the fast ions carry the neutral-beam-driven current, high fast ion pressure is required in order to drive a significant fraction of  $I_p$ ,  $f_B \approx 0.4$ –0.5. The fast ion pressure increases linearly with  $P_B$  and also increases with  $T_e$  (as shown by the scaling described in the appendix). In contrast, assuming IPB98(y,2) confinement scaling, the thermal plasma pressure increases more slowly,  $\propto P_H^{0.31}$ . In the example of Fig. 8, as the neutral beam power increases in order to increase  $\beta_N$  by 47% (from 3.4 to 5),  $\beta_{Nth}$  increases only 17% while the component resulting from the fast ion pressure,  $\beta_{Nf}$ , increases by a factor of 2; and, at the  $f_{NI} = 1$  solution,  $\beta_{Nf}/\beta_N \approx 0.4$ . The fast ion pressure remains near 40% of the total pressure as  $q_{95}$ ,  $B_T$ , and  $n_e$  are varied.

A shift of a fraction of the neutral beam power to off-axis injection makes a relatively small difference in the  $f_{NI} = 1$  operating point (Fig. 9 dotted-dashed line compared to the solid line). The fast ion stored energy fraction decreases slightly as a result of the difference in  $n_e$  and  $T_e$  between the axis and the mid-radius, but the total neutral-beam-driven current remains the same as a result of reduced electron shielding at mid-radius.<sup>19</sup> The result is slightly lower  $\beta_N$  to achieve the same  $\beta_{Nth}$ . With less neutral-beam-driven current density in the region near the axis,  $q_{core}$  increases [Fig. 9(b)].  $f_{BS}$  remains the same, though, because the model input value of  $f_{pi}$  for cases with off-axis injection reflects a decrease in the pressure gradient near the axis that matches the experimentally observed broadening of the pressure profile.

A substantial increase in the EC power can make a significant change in the discharge parameters at  $f_{NI} = 1$  by driving current without producing a large fast particle pressure. With the EC power configured to drive current off-axis, as is the case in all of the discharges discussed thus far, the value of  $\beta_N$  at the  $f_{NI} = 1$  solution decreases as a result of a decrease in the fast ion pressure (Fig. 12, solid lines). As  $P_{EC}$  increases, EC driven current replaces neutral beam driven current sufficiently well that  $\beta_{Nth}$  and  $P_H$  [Figs. 12(a) and 12(d)] remain approximately constant while  $P_B$  decreases. (The EC power is assumed to heat the thermal plasma as

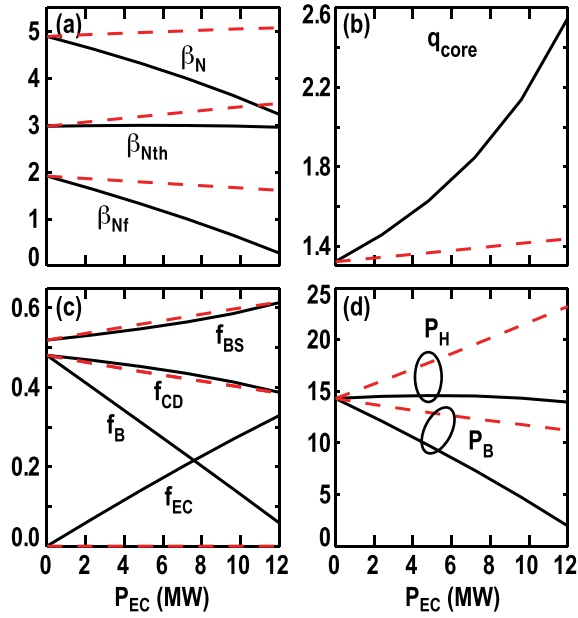


FIG. 12. Parameters at the  $f_{NI} = 1$  operating point as a function of  $P_{EC}$  obtained using the 0-D model. (a)  $\beta_N$ ,  $\beta_{Nth}$ , and  $\beta_{Nf}$ , (b)  $q_{core}$ , (c) the noninductive current fractions, and (d) the input powers. For the solid line, the EC power drives current off-axis; and for the dashed line, the EC power is modeled as providing heating only, without driving current (so  $f_{CD} = f_B$ ,  $f_{EC} = 0$ ).  $P_{offaxis} = 0$ ,  $f_{pi} = 1.35$ ,  $f_{po} = 1.25$ ,  $T_i(0.13)/T_e(0.13) = 1.35$  at zero EC power ramped to 1.2 at the maximum EC power,  $H_{98} = 1.5$ .

efficiently as neutral beam power.) The bootstrap current fraction at this constant  $P_H$  increases somewhat because  $q_{core}$  increases as the neutral beam driven current near the axis decreases. Thus, it can be much easier to satisfy MHD stability requirements as  $\beta_N$  in the fully noninductive solution drops from  $\approx 5$  with zero EC power to  $\approx 3.3$  at the maximum power shown. Note that there are quantitative uncertainties in these projections as a result of the use of EC power well outside the range that has been used thus far at DIII-D.

An approach to achieving a bootstrap current fraction near 1 is to use a source of substantial heating power that does not drive current. This could yield a  $f_{NI} = 1$  solution with  $\beta_N \approx 5$  and  $\beta_T$  in the range required for a high Q burning plasma. Heating power of this type will come from alpha self-heating in a reactor. A projection of this scenario for DIII-D can be made by treating the EC power as a source of heating only (which would be the case with perpendicular injection), as illustrated by the dashed lines in Fig. 12. As  $P_{EC}$  is increased, the neutral-beam-driven current is replaced by bootstrap current as  $\beta_{Nth}$  increases. The required  $P_B$  drops as does the fast ion pressure. However, with the slow,  $\propto P_H^{0.31}$ , increase of the thermal stored energy, the decrease in  $P_B$  with increasing  $P_{EC}$  is slow. Even with the relatively high  $H_{98} = 1.5$  assumed, to reach  $f_{BS} \approx 0.9$  (where  $f_{NI} = 1$  and  $\beta_N \approx 5.2$ ),  $P_{EC} \approx 60$  MW is required, well beyond the range considered in Fig. 12. Another possible source of heating power that would drive little current is neutral beam injection balanced in the co and counter plasma current directions. The power required in this case would be comparable to what is required with EC heating, but, because a substantial fast ion population would be introduced,  $\beta_N$  at  $f_{NI} = 1$  would be higher.

## VI. A $\beta_N = 5$ SOLUTION FROM A 1-D MODEL

In this section, we describe how off-axis neutral beam injection could be combined with off-axis ECCD to produce an MHD stable plasma in DIII-D with  $\beta_N \approx 5$ . To project to this type of discharge, a 1-D model was used to study weak shear  $q$  profiles with  $q_{min} > 2$  and the radius of the minimum in  $q$ ,  $\hat{\rho}_{q_{min}}$ , as large as possible. This approach results in a current density profile with peak value well away from the magnetic axis to maximize the stabilizing effect of the conducting vacuum vessel wall. In addition, the majority of the additional neutral beam power required to raise  $\beta_N$  is injected off-axis in order to produce a broad fast ion pressure profile and contribute to broadening the current profile. An increase in the available ECCD power to 9 MW was assumed, with the role of the ECCD in this modeling to provide current drive as far off-axis as possible while still maintaining a reasonable current drive efficiency. An increase in the available off-axis co-injected neutral beam power to 14 MW is also assumed. The plasma current was held constant with  $B_T = 1.75$  T to fix  $q_{95}$  at 5.5. Anomalous fast ion diffusion  $D_f = 0.3$  m<sup>2</sup>/s was applied in the neutral beam model NUBEAM.<sup>25</sup>

In order to design this discharge scenario, the transport code ONETWO<sup>28</sup> is used with the TGLF<sup>37</sup> transport model to predict the electron and ion temperature profiles. The temperature profiles in the H-mode pedestal,  $\hat{\rho} > 0.8$ , are based on a previous DIII-D discharge (147634) as is the complete density profile. An iterative numerical procedure is employed that finds a stationary solution ( $d/dt = 0$ ) of core transport using FASTRAN.<sup>38</sup> This approach was benchmarked against the database of DIII-D steady-state scenario discharges, with the result that the stored energy and  $f_{BS}$  were predicted within 15%, although the temperature profiles and gradients are not always accurately reproduced.<sup>26</sup> This 1-D method has the advantage over the 0-D model of allowing calculation of the current density<sup>25,29–31</sup> and pressure profiles using realistic current drive and heating power sources. Deposition profiles for the externally driven current can be varied in order to determine the power requirements to produce a particular  $q$  profile. In addition, the code produces a self-consistent equilibrium<sup>27</sup> that was tested against the ideal stability codes GATO<sup>39</sup> and DCON.<sup>34</sup> The stability limit is defined here as the maximum stable  $\beta_N$  for ideal  $n = 1$ ,  $n = 2$ , and  $n = 3$  modes in the presence of a perfectly conducting wall at the location of the DIII-D vacuum vessel.

The MHD stable, stationary equilibrium solution found with the 1-D model has  $\beta_N = 4.94$  and both a broad pressure profile, with  $f_p \approx 2.7$ , and a broad current density profile, with the peak at  $\hat{\rho} \approx \hat{\rho}_{q_{min}} \approx 0.6$  [Fig. 13(a)]. In contrast, in current experiments, although  $f_p$  is about the same, the radius of the current density peak is much smaller  $\hat{\rho} \approx 0.3$  [Fig. 13(c)]. A change in the discharge shape, from the high average triangularity, single-null divertor shape used in present experiments to maximize divertor exhaust pumping<sup>20</sup> (with elongation  $\kappa \approx 1.8$ ) to an up-down symmetric double null divertor ( $\kappa \approx 2$ ) also contributes an improvement to MHD stability. The noninductive current [Fig. 13(b)] is a combination of the EC driven current  $J_{EC}$  ( $f_{EC} = 0.17$ ), neutral-beam-driven

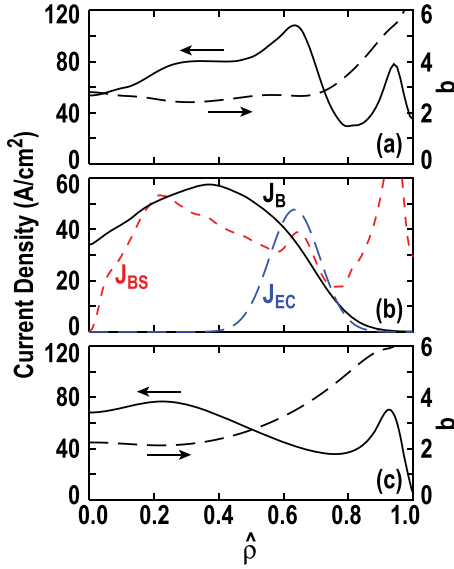


FIG. 13. (a) Current density (solid curve) and safety factor (dashed curve) profiles in the  $\beta_N = 4.94$  equilibrium calculated using the 1-D model. (b) The noninductive current density profiles corresponding to the total current density in (a). (c) The current density (solid curve) and safety factor (dashed curve) profiles in an experimental discharge with  $q_{\min} > 2$ ,  $\beta_N = 3$  and off-axis neutral beam injection (146821).

current  $J_B$  peaking at  $\hat{\rho} \approx 0.4$  ( $f_B = 0.43$ ), and a relatively large bootstrap current density  $J_{BS}$  at this high value of  $\beta_N$  ( $f_{BS} = 0.56$ ). With  $\beta_N = 4.94$ , the total noninductive current fraction is above 1,  $f_{NI} = 1.16$ , in agreement with the projection of the 0-D analysis for  $q_{95} = 5.5$  (Fig. 9). Further tuning of the model equilibrium to find  $f_{NI}$  closer to 1 at  $\beta_N = 5$  should, according to the 0-D model, shift  $q_{95}$  to a lower value.

## VII. CONCLUSION

The initial experiments on off-axis neutral beam injection into DIII-D high  $\beta_N$  discharges have demonstrated changes in the plasma profiles in the direction toward increased limits to plasma pressure as determined by ideal low- $n$  MHD instabilities. Both the current density and plasma pressure profiles were broadened. Discharges could be produced with  $q_{\min}$  maintained above 2 as a result of a shift of neutral-beam-driven current from on-axis to off-axis. The broader pressure profiles led to an increase in the calculated  $\beta_N$  limit for experimental discharges with  $\ell_i > 0.7$  to values above 4.5. Confinement of the thermal plasma with off-axis injection was found to be comparable to what is expected for H-mode. Global confinement, though, appears to be reduced when  $q_{\min}$  is above 2 so that the experimental values of  $\beta_N$  in this range of  $q_{\min}$  have thus far been limited to a maximum of 3.3. At lower  $q_{\min}$ , a test of the effect on global confinement of the shift in neutral beam deposition location to off-axis showed only a small reduction.

We have described an approach to a steady-state scenario with  $\beta_T$  in the range required for a reactor in which broad pressure and current profiles enable stability at high normalized pressure, and, self-consistently, the high pressure is required in order to reach  $f_{NI} = 1$ . The 0-D model was used to show that steady-state solutions in DIII-D require  $\beta_N$  in the range 4–5 in discharges with a broad pressure profile.

This is the case over the full range of  $q_{95}$ ,  $B_T$ , and  $n_e$  appropriate for DIII-D. A projected fully noninductive solution at  $\beta_N \approx 5$  and  $\beta_T \approx 6.5\%$  was found at  $q_{95} \approx 4$ . The 1-D model was used to show that broadening of the current density profile beyond what has thus far been achieved in the experiment in relatively stationary conditions, while maintaining the weak-shear  $q$  profile shape along with the predicted broad pressure profile, can lead to MHD stable discharges in this range of  $\beta_N$ . A fully noninductive solution at  $\beta_N \approx 5$  and  $q_{95} = 5.5$  that could be demonstrated in DIII-D with an increase in the available heating and current drive power was described. Although the numerical results found from the models will be specific to DIII-D, the parametric dependences of  $f_{NI} = 1$  solutions should apply to the current generation of tokamaks.

An issue that has not yet been resolved in the experiment is the role of fast ion transport. The data presented here provide some evidence that the anomalous fast ion behavior at the highest values of  $q_{\min}$  is a result of interactions with Alfvén eigenmode type instabilities. It is not yet known, though, to what extent behavior that differs from the NUBEAM model is a result of anomalously rapid slowing down, radial redistribution of fast ions, or fast ion loss. In addition, it is not yet known whether the fast ion diffusion model in NUBEAM is a good representation of the experimental behavior. Because of this, fast ion diffusion was not included in the discussion of the 0-D model and only a small fast ion diffusivity was included in the 1-D model. The most significant consequence could be an under prediction of the required neutral beam power by the model. Detailed measurements of the fast ion profiles and the profile of the current density driven by the off-axis neutral beams in high  $\beta_N$  discharges and comparison with the NUBEAM model are planned in order to improve understanding of the fast ion behavior. A further goal of additional experiments will be to determine the parameter regimes where the fast ion stored energy is the closest to the NUBEAM-predicted value in order to improve the global confinement, or to find regimes where fast ion loss can be compensated by improvements in thermal confinement.

The reactor-relevant physics of current drive, bootstrap current generation, and maintenance of stable, stationary, steady-state discharges can be studied in the current generation of tokamaks, but the combinations of  $f_{BS}$  and  $\beta_N$  will differ from what would be expected in a burning plasma. A comparison can be made, for example, to the Aries-AT study which found<sup>4</sup> an optimized steady-state reactor design at  $f_{BS} = 0.91$  and  $\beta_N = 5.4$  by maintaining high thermal plasma pressure. The current tokamak generation lacks the necessary high alpha self-heating power that overcomes the slow scaling of thermal stored energy with input power. As shown here, with the broad pressure profile that enables the self-consistent,  $f_{NI} = 1$  solution to be at  $\beta_N \approx 5$ , at  $f_{NI} = 1$  the bootstrap current fraction is limited to a value near 0.5. This will be the case even as  $q_{\min}$  is increased because the thermal pressure profile broadens simultaneously, reducing the pressure gradient in the region where  $q \approx q_{\min}$ . If an ITB-type pressure profile with steeper gradients is present,  $f_{BS}$  can be larger, but at  $f_{NI} = 1$ ,  $\beta_N$  is reduced. Thus, the

current options are either high  $\beta_N$  combined with lower than desired  $f_{BS}$ , or higher  $f_{BS}$  combined with relatively low  $\beta_N$ . In both cases, MHD stability and good alignment of the non-inductive and total current profiles must be considered. The Aries-AT design combines these two approaches with  $q_{\min} > 2$  and  $q(0) - q_{\min} \approx 1$ , but with  $\hat{\rho}_{q_{\min}} \approx 0.8$  and a very broad pressure profile. In this way, most of the pressure gradient is located in the outer half of the discharge and the bootstrap current density profile is broad with the peak close to the boundary. DIII-D experiments are pointing in this same direction through the use of off-axis neutral beam and EC current drive to simultaneously produce both broad pressure and current density profiles. The aim of this line of research is to provide the physics basis for steady-state operation in ITER and later facilities such as FNSF and a demonstration reactor.

## ACKNOWLEDGMENTS

This work was supported in part by the US Department of Energy under DE-FC02-04ER54698, DE-AC52-07NA27344, DE-AC05-00OR22725, DE-FG02-04ER54761, SC-G903402, DE-FG02-08ER54984, DE-FG02-06ER84442, and DE-AC02-09CH11466.

## APPENDIX: DESCRIPTION OF THE 0-D MODEL

The 0-D model is composed of a series of easily evaluated analytic expressions for  $f_{BS}$ ,  $f_B$ ,  $f_{EC}$  and quantities on which these values depend. Each of the expressions contains free parameters (represented here by  $C_n$ ) that are determined through fits to the database of DIII-D discharges described in Sec. II.

The profiles of  $J_B$ , the ECCD current density  $J_{EC}$ , and the fast ion pressure do not vary significantly over the range of parameters used for DIII-D steady-state scenario discharges, except for changes that result from off-axis neutral beam injection. Therefore,  $f_B$ ,  $f_{EC}$ , and the total fast ion stored energy,  $W_f$ , can be well represented as proportional to the current density or pressure evaluated at a single radius chosen to minimize the  $\chi^2$  of the fit to the database. The key radii are  $\hat{\rho} = 0.13, 0.4$ , and  $0.5$ . Estimates of  $T_e$  at these locations are obtained from  $\langle P_{th} \rangle$ , the local  $n_e$ , and model input values of  $T_i/T_e$  and the thermal pressure peaking factors for the inner and outer portions of the discharge,  $f_{pi} = [P_{th}(0.13) - P_{th}(0.5)]/\langle P_{th} \rangle$  and  $f_{po} = P_{th}(0.5)/\langle P_{th} \rangle$ . Estimates of  $n_e(0.13)$  and  $n_e(0.5)$  are obtained using model input values of the main ion density and  $Z_{\text{eff}}$ , and estimates of the local fast ion density from fits to  $P_B \tau_{se}/E_B$ , the product of the local fast ion thermalization time<sup>40</sup> and the volume average fast ion source rate, where  $E_B$  is the neutral beam injection energy.

The bootstrap current fraction is modeled as the sum of two terms representing the bootstrap current in the inner and outer halves of the plasma, similarly to what was described previously:<sup>21</sup>  $f_{BS} = \beta_{Nth}(C_1 q_{\text{core}} f_{pi}^{C_2} + C_3 q_{95} f_{po}^{C_4})$ . A difference from the previous method<sup>21</sup> is the use of separate peaking factors that account for broadening of the thermal pressure profile with off-axis neutral beam injection and the

corresponding changes in the profile shape. The average value of  $q$  in the region  $0 < \hat{\rho} < 0.3$  is  $q_{\text{core}} = C_5 B_T / J_{\text{core}}$ , where  $J_{\text{core}}$  is the sum of the average bootstrap, beam-driven and inductively generated (zero at  $f_{NI} = 1$ ) currents in the region  $0 < \hat{\rho} < 0.13$ , a region chosen to minimize the  $\chi^2$  of this fit.

The neutral-beam-driven current density estimate is based on Eq. (15) of the neutral beam current drive model in Ref. 41

$$\tilde{J}_B = \left[ \frac{P_B Z_B^2 \tau_{se}}{V \sqrt{A_B E_c}} \right] J(E_B, E_c, \dots) F(Z_B, Z_{\text{eff}}, \epsilon). \quad (\text{A1})$$

Here,  $Z_B$  and  $A_B$  are the charge and mass of the fast ions,  $\epsilon = a/R$  is the inverse aspect ratio, the ion-electron slowing down time  $\tau_{se}$  and the critical energy  $E_c$  are defined in Ref. 41,  $J$  accounts for slowing down on both ions and electrons,  $F$  includes the effect of trapping on the electron shielding current ( $J$  and  $F$  are defined in Ref. 41), and the term in brackets times  $J$  increases with  $T_e/n_e$  in the DIII-D parameter range. The neutral beam current drive fraction is  $f_B = C_6 \tilde{J}_B(0.5)(q_{95}/B_T)$ .

A model for the fast ion stored energy is obtained by integrating the steady-state solution to the pitch angle averaged Fokker-Planck equation  $f(v) = (P_B \tau_{se}/E_B)/(v^3 + v_c^3)$  to obtain

$$\begin{aligned} \tilde{W}_f(P_B, T_e, n_e, \dots) &= \frac{P_B \tau_{se}}{2} \left\{ 1 + \frac{2}{3} \left( \frac{v_c}{v_B} \right)^2 \left[ \frac{1}{2} \ln \left[ \frac{(v_B + v_c)^2}{v_B^2 - v_B v_c + v_c^2} \right] \right. \right. \\ &\quad \left. \left. - \sqrt{3} \left[ \frac{\pi}{6} + \tan^{-1} \left( \frac{2v_B - v_c}{\sqrt{3}v_c} \right) \right] \right] \right\}. \end{aligned} \quad (\text{A2})$$

Here,  $v_B = \sqrt{2E_B/A_B m_p}$  is the neutral beam injection velocity, and  $v_c = \sqrt{2E_c/A_B m_p}$  is the critical velocity ( $m_p$  is the mass of a proton). The total fast ion stored energy is the sum of contributions from the on-axis and off-axis neutral beams,  $W_f = C_7 \tilde{W}_f(P_B - P_{\text{offaxis}}, T_e(0.13), n_e(0.13), \dots) + C_8 \tilde{W}_f(P_{\text{offaxis}}, T_e(0.5), n_e(0.5), \dots)$ .

The fraction of  $I_p$  resulting from ECCD,  $f_{EC}$ , is

$$f_{EC} = \frac{P_{EC} T_e(0.4)}{n_e(0.5)} [C_9 + C_{10} \hat{\rho}_{EC}] [C_{11} + C_{12} (\bar{R}_m - R_{EC})] \frac{q_{95}}{B_T}, \quad (\text{A3})$$

where  $\bar{R}_m$  is the average major radius of the magnetic axis and  $R_{EC}$  is the major radius of the EC resonance. The dependence on  $n_e$  and  $T_e$  matches the description in Ref. 42. The two terms in brackets are linearizations within the range of the database that represent the dependence on the average radius of the EC deposition,  $\hat{\rho}_{EC}$ , and a reduction in the current drive efficiency as the resonance location moves from smaller to larger major radius where the electron trapping fraction is higher.

<sup>1</sup>T. C. Luce, *Phys. Plasmas* **18**, 030501 (2011).

<sup>2</sup>C. Gomezano, A. C. C. Sips, T. C. Luce, S. Ide, A. Becoulet, X. Litaudon, A. Isayama, J. Hobbirk, M. R. Wade, T. Oikawa, R. Prater, A. Zvonkov,

- B. Lloyd, T. Suzuki, E. Barbato, P. Bonoli, C. K. Phillips, V. Vdovin, E. Joffrin, T. Casper, J. Ferron, D. Mazon, D. Moreau, R. Budny, C. Kessel, A. Fukuyama, N. Hayashi, F. Imbeaux, M. Murakami, A. R. Polevoi, and H. E. St. John, *Nucl. Fusion* **47**, S285 (2007).
- <sup>3</sup>V. S. Chan, R. D. Stambaugh, A. M. Garofalo, M. S. Chu, R. K. Fisher, C. M. Greenfield, D. A. Humphreys, L. L. Lao, J. A. Leuer, T. W. Petrie, R. Prater, G. M. Staebler, P. B. Snyder, H. E. St. John, A. D. Turnbull, C. P. C. Wong, and M. A. Van Zeeland, *Fusion Sci. Technol.* **57**, 66 (2010).
- <sup>4</sup>F. Najmabadi, ARIES Team, A. Abdou, L. Bromberg, T. Brown, V. C. Chan, M. C. Chu, F. Dahlgren, L. El-Guebaly, P. Heitzenroeder, D. Henderson, H. E. St. John, C. E. Kessel, L. L. Lao, G. R. Longhurst, S. Malang, T. K. Mau, B. J. Merrill, R. L. Miller, E. Mogaheed, R. L. Moore, T. Petrie, D. A. Petti, P. Politzer, A. R. Raffray, D. Steiner, I. Sviatoslavsky, P. Synder, G. M. Syaebler, A. D. Turnbull, M. S. Tillack, L. M. Waganer, X. Wang, P. West, and P. Wilson, *Fusion Eng. Des.* **80**, 3 (2006).
- <sup>5</sup>J. L. Luxon, *Fusion Sci. Technol.* **48**, 828 (2005).
- <sup>6</sup>J. R. Ferron, T. A. Casper, E. J. Doyle, A. M. Garofalo, P. Gohil, C. M. Greenfield, A. W. Hyatt, R. J. Jayakumar, C. Kessel, J. Y. Kim, T. C. Luce, M. A. Makowski, J. Menard, M. Murakami, C. C. Petty, P. A. Politzer, T. S. Taylor, and M. R. Wade, *Phys. Plasmas* **12**, 056126 (2005).
- <sup>7</sup>W. Howl, A. D. Turnbull, T. S. Taylor, L. L. Lao, F. J. Helton, J. R. Ferron, and E. J. Strait, *Phys. Fluids B* **4**, 1724 (1992).
- <sup>8</sup>A. D. Turnbull, T. S. Taylor, M. S. Chu, R. L. Miller, and Y. R. Lin-Liu, *Nucl. Fusion* **38**, 1467 (1998).
- <sup>9</sup>ITER Physics Basis Editors, "ITER physics expert group on confinement and transport and confinement modeling and database," *Nucl. Fusion* **39**, 2175 (1999).
- <sup>10</sup>P. N. Yushmanov, T. Takizuka, K. S. Riedel, O. J. W. F. Kardaun, J. G. Cordey, S. M. Kaye, and D. E. Post, *Nucl. Fusion* **30**, 1999 (1990).
- <sup>11</sup>A. D. Turnbull, T. S. Taylor, Y. R. Lin-Liu, and H. St. John, *Phys. Rev. Lett.* **74**, 718 (1995).
- <sup>12</sup>A. M. Garofalo, E. J. Doyle, J. R. Ferron, C. M. Greenfield, R. J. Groebner, A. W. Hyatt, G. L. Jackson, R. J. Jayakumar, J. E. Kinsey, R. J. La Haye, G. R. McKee, M. Murakami, M. Okabayashi, T. H. Osborne, C. C. Petty, P. A. Politzer, H. Reimerdes, J. T. Scoville, W. M. Solomon, H. E. St. John, E. J. Strait, A. D. Turnbull, M. R. Wade, and M. A. Van Zeeland, *Phys. Plasmas* **13**, 056110 (2006).
- <sup>13</sup>T. C. Hender, J. C. Wesley, J. Bialek, A. Bondeson, A. H. Boozer, R. J. Buttery, A. Garofalo, T. P. Goodman, R. S. Granetz, Y. Gribov, O. Gruber, M. Gryaznevich, G. Giruzzi, S. Gunter, N. Hayashi, P. Helander, C. C. Hegna, D. F. Howell, D. A. Humphreys, G. T. A. Huysmans, A. W. Hyatt, A. Isayama, S. C. Jardin, Y. Kawano, A. Kellman, C. Kessel, H. R. Koslowski, R. J. La Haye, E. Lazzaro, Y. Q. Liu, V. Lukash, J. Manickam, S. Medvedev, V. Mertens, S. V. Mironov, Y. Nakamura, G. Navratil, M. Okabayashi, T. Ozeki, R. Paccagnella, G. Pautasso, F. Porcelli, V. D. Pustovitov, V. Riccardo, M. Sato, O. Sauter, M. J. Schaffer, M. Shimada, P. Sonato, E. J. Strait, M. Sugihara, M. Takechi, A. D. Turnbull, E. Westerhof, D. G. Whyte, R. Yoshino, H. Zohm, and ITPA MHD, Disruption and Magnetic Control Topical Group, *Nucl. Fusion* **47**, S128 (2007).
- <sup>14</sup>F. M. Poli, C. E. Kessel, M. S. Chance, S. C. Jardin, and J. Manickam, *Nucl. Fusion* **52**, 063027 (2012).
- <sup>15</sup>T. Suzuki, R. J. Akers, D. A. Gates, S. Gunter, W. W. Heidbrink, J. Hobbirk, T. C. Luce, M. Murakami, J. M. Park, M. Turnyanskiy, and ITPA "Integrated Operation Scenarios group members and experts," *Nucl. Fusion* **51**, 083020 (2011).
- <sup>16</sup>J. Hobbirk, T. Oikawa, T. Fujita, T. Fukuda, S. Gunter, O. Gruber, A. Isayama, Y. Kamada, M. Kikuchi, M. Maraschek, Y. Miura, A. G. Peeters, G. V. Pereverzev, A. Polevoi, A. C. C. Sips, A. Staebler, J. Stober, T. Suzuki, K. Ushigusa, and ASDEX Upgrade Team and JT-60U Team, in Proc. 30th EPS Conf. on Controlled Fusion and Plasma Physics, St. Petersburg, Russia (ECA, 2003), Vol. 27A, O-4.1B.
- <sup>17</sup>M. Turnyanskiy, D. L. Keeling, R. J. Akers, G. Cunningham, N. J. Conway, H. Meyer, C. A. Michael, and S. D. Pinches, *Nucl. Fusion* **49**, 065002 (2009).
- <sup>18</sup>T. Suzuki, N. Oyama, A. Isayama, Y. Sakamoto, T. Fujita, S. Ide, Y. Kamada, O. Naito, M. Sueoka, S. Moriyama, M. Hanada, and JT-60 Team, *Nucl. Fusion* **49**, 085003 (2009).
- <sup>19</sup>M. Murakami, J. M. Park, C. C. Petty, T. C. Luce, W. W. Heidbrink, T. H. Osborne, R. Prater, M. R. Wade, P. M. Anderson, M. E. Austin, N. H. Brooks, R. V. Budny, C. D. Challis, J. C. DeBoo, J. S. deGrassie, J. R. Ferron, P. Gohil, J. Hobbirk, C. T. Holcomb, E. M. Hollmann, R. M. Hong, A. W. Hyatt, J. Lohr, M. J. Lanctot, M. A. Makowski, D. C. McCune, P. A. Politzer, J. T. Scoville, H. E. St. John, T. Suzuki, W. P. West, E. A. Unterberg, M. A. Van Zeeland, and J. H. Yu, *Nucl. Fusion* **49**, 065031 (2009).
- <sup>20</sup>C. T. Holcomb, J. R. Ferron, T. C. Luce, T. W. Petrie, P. A. Politzer, C. Challis, J. C. DeBoo, E. J. Doyle, C. M. Greenfield, R. J. Groebner, M. Groth, A. W. Hyatt, G. L. Jackson, C. Kessel, R. J. La Haye, M. A. Makowski, G. R. McKee, M. Murakami, T. H. Osborne, J.-M. Park, R. Prater, G. D. Porter, H. Reimerdes, T. L. Rhodes, M. W. Shafer, P. B. Snyder, A. D. Turnbull and W. P. West, *Phys. Plasmas* **16**, 056116 (2009).
- <sup>21</sup>J. R. Ferron, C. Holcomb, T. C. Luce, P. Politzer, F. Turco, A. White, J. DeBoo, E. Doyle, A. Hyatt, R. La Haye, T. Petrie, C. Petty, T. Rhodes, and L. Zeng, *Nucl. Fusion* **51**, 063026 (2011).
- <sup>22</sup>M. A. Van Zeeland, W. W. Heidbrink, J. M. Park, R. Prater, C. T. Holcomb, M. E. Austin, J. R. Ferron, C. M. Greenfield, B. A. Grierson, R.-M. Hong, T. C. Luce, G. R. McKee, R. A. Moyer, M. Murakami, C. J. Murphy, C. M. Muscatello, D. C. Pace, C. C. Petty, J. Rauch, J. T. Scoville, W. M. Solomon, and B. J. Tobias, in Proc. 39th EPS Conf. on Controlled Fusion and Plasma Physics, Stockholm, Sweden (ECA, 2012), Vol. 36F, P2.068.
- <sup>23</sup>W. W. Heidbrink, M. A. Van Zeeland, B. A. Grierson, C. M. Muscatello, J. M. Park, C. C. Petty, R. Prater, and Y. B. Zhu, *Nucl. Fusion* **52**, 094005 (2012).
- <sup>24</sup>J. M. Park, E. J. Doyle, J. R. Ferron, C. T. Holcomb, G. L. Jackson, L. L. Lao, T. C. Luce, L. W. Owen, M. Murakami, T. H. Osborne, P. A. Politzer, R. Prater, and P. B. Snyder, in Proc. 24th IAEA Fusion Energy Conf., San Diego, 2012, Paper EX/P2-13.
- <sup>25</sup>A. Pankin, D. McCune, R. Andre, G. Bateman, and A. Kritiz, *Comput. Phys. Commun.* **159**, 157 (2004).
- <sup>26</sup>F. Turco, C. T. Holcomb, J. R. Ferron, T. C. Luce, P. A. Politzer, J. M. Park, A. E. White, D. P. Brennan, A. D. Turnbull, J. M. Hanson, M. Okabayashi, and Y. In, *Phys. Plasmas* **19**, 122506 (2012).
- <sup>27</sup>L. L. Lao, J. R. Ferron, R. J. Groebner, W. Howl, H. St. John, E. J. Strait, and T. S. Taylor, *Nucl. Fusion* **30**, 1035 (1990).
- <sup>28</sup>H. E. St. John, T. S. Taylor, Y. R. Lin-Liu, and A. D. Turnbull, in *Proceedings of the 15th International Conference on Plasma Physics and Controlled Nuclear Research, Seville, Spain, 1994* (IAEA, Vienna, 1995), Vol. 3, p. 603.
- <sup>29</sup>O. Sauter, C. Angioni, and Y. R. Lin-Liu, *Phys. Plasmas* **6**, 2834 (1999).
- <sup>30</sup>O. Sauter, C. Angioni, and Y. R. Lin-Liu, *Phys. Plasmas* **9**, 5140 (2002).
- <sup>31</sup>Y. R. Lin-Liu, V. S. Chan, and R. Prater, *Phys. Plasmas* **10**, 4064 (2003).
- <sup>32</sup>J. R. Ferron, C. T. Holcomb, T. C. Luce, P. A. Politzer, F. Turco, J. C. DeBoo, E. J. Doyle, Y. In, R. J. La Haye, M. Murakami, M. Okabayashi, J. M. Park, T. W. Petrie, C. C. Petty, and H. Reimerdes, *Nucl. Fusion* **51**, 113007 (2011).
- <sup>33</sup>L. L. Lodestro and L. D. Pearlstein, *Phys. Plasmas* **1**, 90 (1994).
- <sup>34</sup>A. H. Glasser and M. S. Chance, *Bull. Am. Phys. Soc.* **42**, 1848 (1997).
- <sup>35</sup>M. A. Van Zeeland, G. J. Kramer, R. Nazikian, H. L. Berk, T. N. Carlstrom, and W. M. Solomon, *Plasma Phys. Controlled Fusion* **47**, L31 (2005).
- <sup>36</sup>M. Murakami, M. R. Wade, C. M. Greenfield, T. C. Luce, J. R. Ferron, H. E. St. John, J. C. DeBoo, W. W. Heidbrink, Y. Luo, M. A. Makowski, T. H. Osborne, C. C. Petty, P. A. Politzer, S. L. Allen, M. E. Austin, K. H. Burrell, T. A. Casper, E. J. Doyle, A. M. Garofalo, P. Gohil, I. A. Gorelov, R. J. Groebner, A. W. Hyatt, R. J. Jayakumar, K. Kajiwara, C. E. Kessel, J. E. Kinsey, R. J. La Haye, L. L. Lao, A. W. Leonard, J. Lohr, T. W. Petrie, R. I. Pinsker, R. Prater, T. L. Rhodes, A. C. C. Sips, G. M. Staebler, T. S. Taylor, M. A. Van Zeeland, G. Wang, W. P. West, L. Zeng, and DIII-D Team, *Phys. Plasmas* **13**, 056106 (2006).
- <sup>37</sup>G. M. Staebler, J. E. Kinsey, and R. E. Waltz, *Phys. Plasmas* **14**, 055909 (2007).
- <sup>38</sup>J. M. Park, E. J. Doyle, J. R. Ferron, C. T. Holcomb, G. L. Jackson, L. L. Lao, T. C. Luce, L. W. Owen, M. Murakami, T. H. Osborne, P. A. Politzer, R. Prater, and P. B. Snyder, in Proc. 23rd IAEA Fusion Energy Conf., Daejeon, Korea, 2010 (IAEA, Vienna, 2010), CD-ROM, Paper EX/P2-05.
- <sup>39</sup>L. C. Bernard, F. J. Helton, and R. W. Moore, *Comput. Phys. Commun.* **24**, 377 (1981).
- <sup>40</sup>T. H. Stix, *Plasma Phys.* **14**, 367 (1972).
- <sup>41</sup>D. R. Mikkelsen and C. E. Singer, *Nucl. Technol. Fusion* **4**, 237 (1983).
- <sup>42</sup>T. C. Luce, Y. R. Lin-Liu, R. W. Harvey, G. Giruzzi, P. A. Politzer, B. W. Rice, J. M. Lohr, C. C. Petty, and R. Prater, *Phys. Rev. Lett.* **83**, 4550 (1999).